

## Supplementary information

### In situ Time Resolved Observation of Intracrystalline Mesoporosity Development in USY Zeolite

Noemi Linares<sup>1</sup>, Alexander Sachse<sup>1</sup>, Elena Serrano<sup>1</sup>, Aida Grau-Atienza<sup>1</sup>, Erika Jardim<sup>1</sup>, Joaquín Silvestre-Albero<sup>2</sup>, Marco Cordeiro<sup>3</sup>, François. Fauth<sup>4</sup>, Garikoitz Beobide<sup>5</sup>, Oscar Castillo<sup>5</sup>, Javier García-Martínez<sup>1,6\*</sup>

<sup>1</sup>Laboratorio de Nanotecnología Molecular, Departamento de Química Inorgánica, Universidad de Alicante, Ctra. San Vicente-Alicante s/n, E-03690 San Vicente del Raspeig, Spain.

<sup>2</sup>Laboratorio de Materiales Avanzados, Departamento de Química Inorgánica-Instituto Universitario de Materiales, Universidad de Alicante, Ctra. San Vicente-Alicante s/n, E-03690 San Vicente del Raspeig, Spain.

<sup>3</sup>Center for Functional Nanomaterials, Brookhaven National Laboratory, Upton, NY 11973, USA.

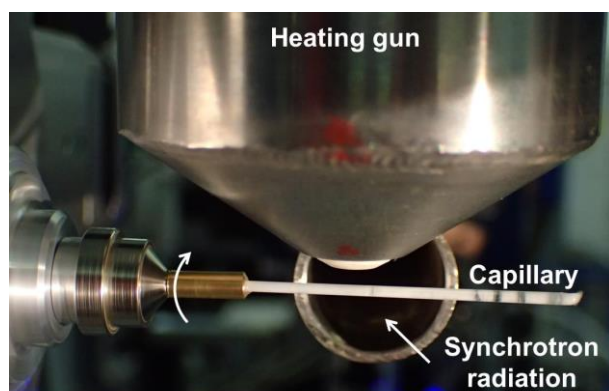
<sup>4</sup>ALBA Light Source, 08290 Cerdanyola del Vallés, Barcelona, Spain.

<sup>5</sup>Departamento de Química Inorgánica, Facultad de Ciencia y Tecnología, Universidad del País Vasco UPV/EHU, Apartado 644, E-48080 Bilbao, Spain.

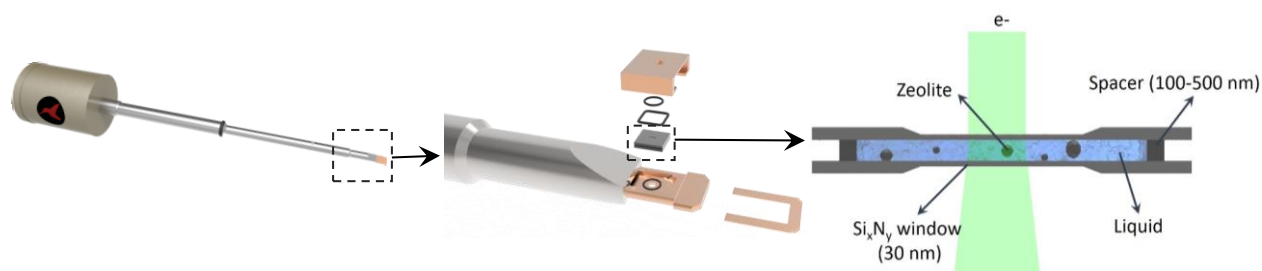
<sup>6</sup>Rive Technology, Inc., 1 Deer Park Drive, Monmouth Junction, NJ 08852, USA.

\*Correspondence and requests for materials should be addressed to J.G.M. (email: [j.garcia@ua.es](mailto:j.garcia@ua.es))

## 1. Methods

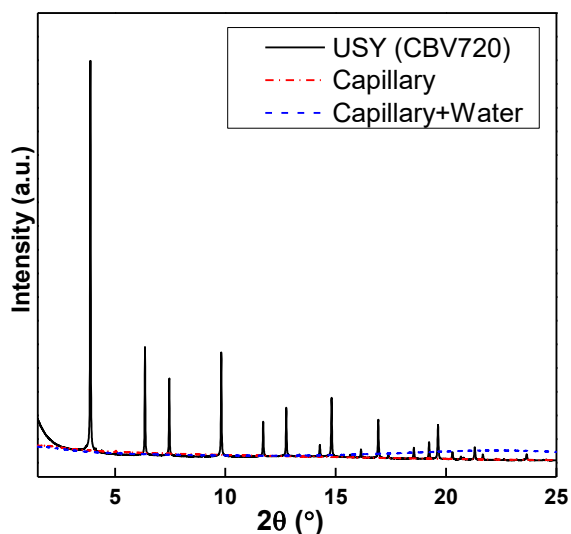


**Supplementary Figure 1.** Optical image of the device used in the powder diffraction station of the BL04-MSPD beamline of the ALBA synchrotron.<sup>1</sup>

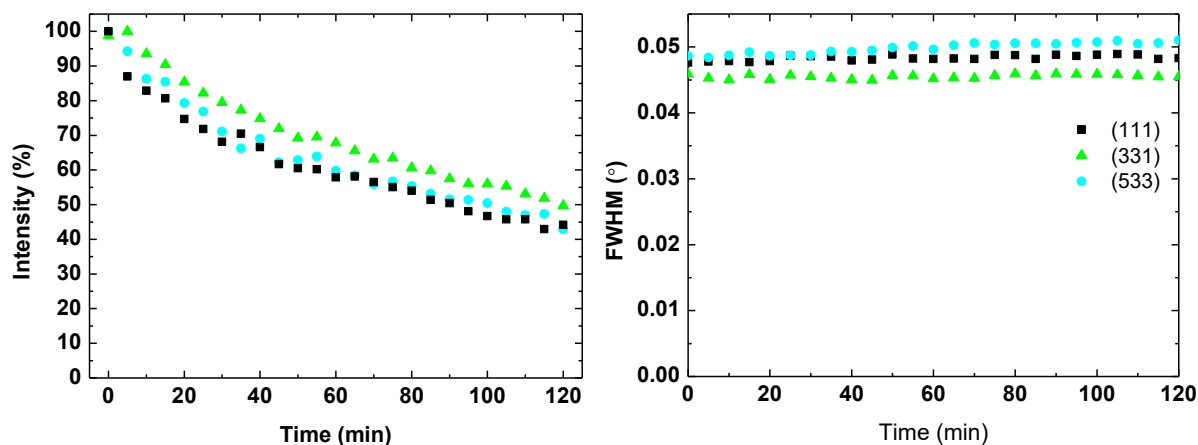


**Supplementary Figure 2.** TEM holder for *in situ* liquid experiments (left), detail of the holder's tip (center) and schematic cross-section of the liquid cell used for Liq-TEM observations (right).

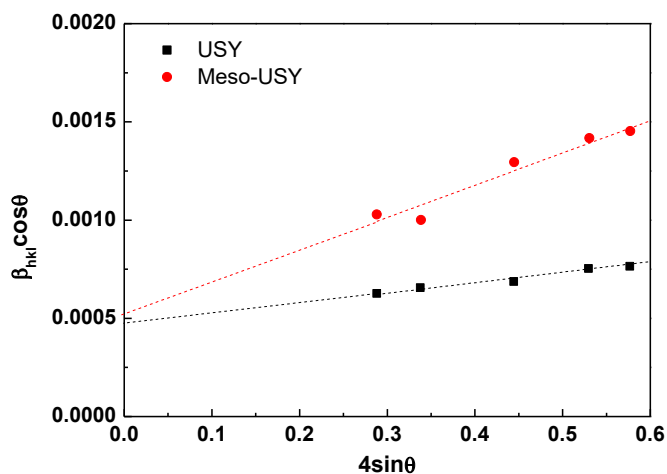
## 2. Control experiments



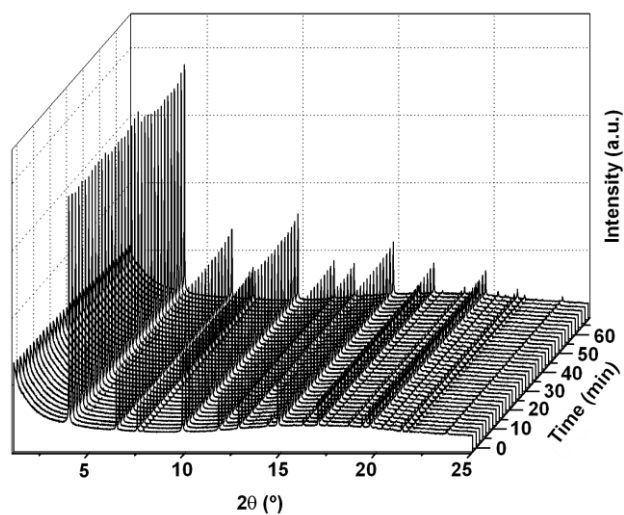
**Supplementary Figure 3.** Synchrotron XRD patterns of parent USY zeolite (capillary filled with the solid sample – black line), the capillary filled with water (dashed blue line) and the empty capillary (dotted red line).



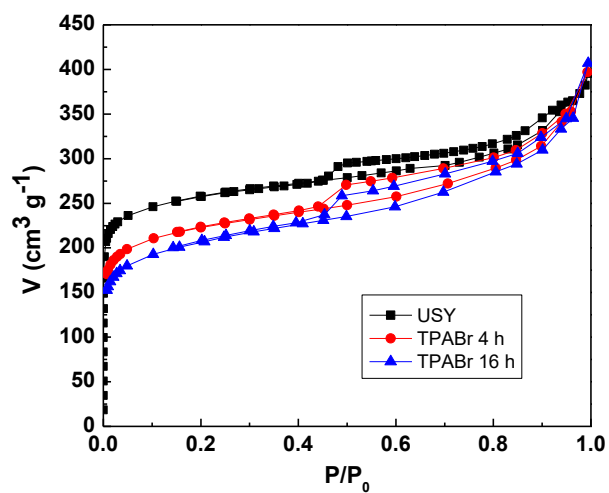
**Supplementary Figure 4.** (Left) Intensity and (right) FWHM evolution of the FAU peaks, corresponding to the (111), (331) and (533) planes, as function of time of USY zeolite surfactant-templating with CTAB at 373 K.



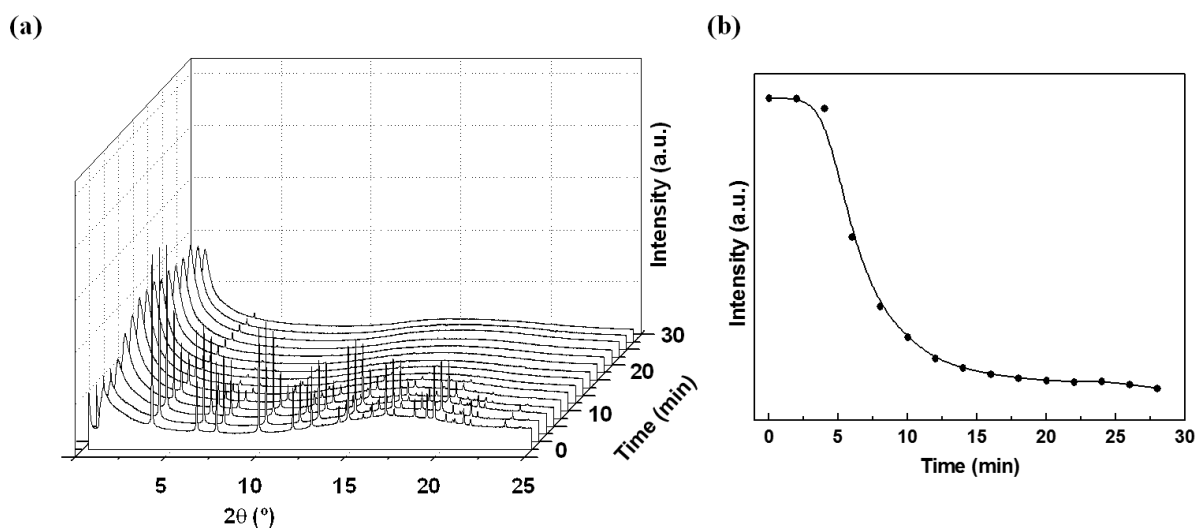
**Supplementary Figure 5.** Williamson-Hall plot representing  $\beta_{hkl}\cos\theta$  vs.  $4\sin\theta$  of calcined surfactant-templated USY zeolite (red circles) and parent USY zeolite (black squares) used to calculate the lattice strain and the crystallite sizes according to the W.-H. analysis.<sup>2</sup>



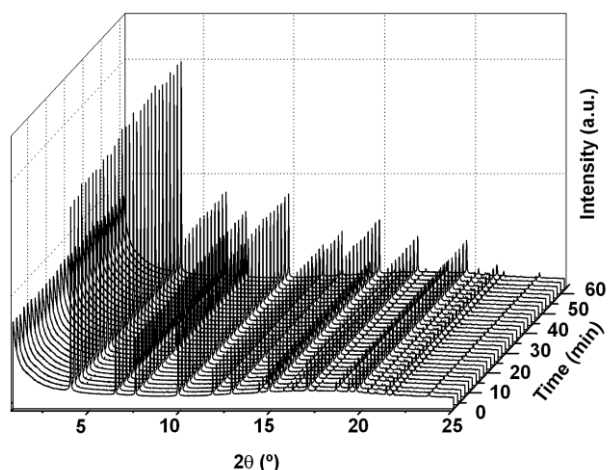
**Supplementary Figure 6.** Time resolved synchrotron XRD patterns of USY zeolite surfactant-templating at 373 K using TPABr.



**Supplementary Figure 7.** Nitrogen adsorption and desorption isotherms recorded at 77 K for the *ex situ* calcined mesoporous USY zeolite prepared using TPABr at 353 K with treatment times of 4 h (red circles) and 16 h (blue triangles) in comparison with the parent USY zeolite (black squares).



**Supplementary Figure 8.** (a) Time resolved synchrotron XRD patterns of USY zeolite treated in basic conditions in the absence of the surfactant. (b) Intensities of the peak at  $3.84^\circ 2\theta$  as function of time.



**Supplementary Figure 9.** Time resolved synchrotron XRD patterns of USY zeolite in water at 373 K.

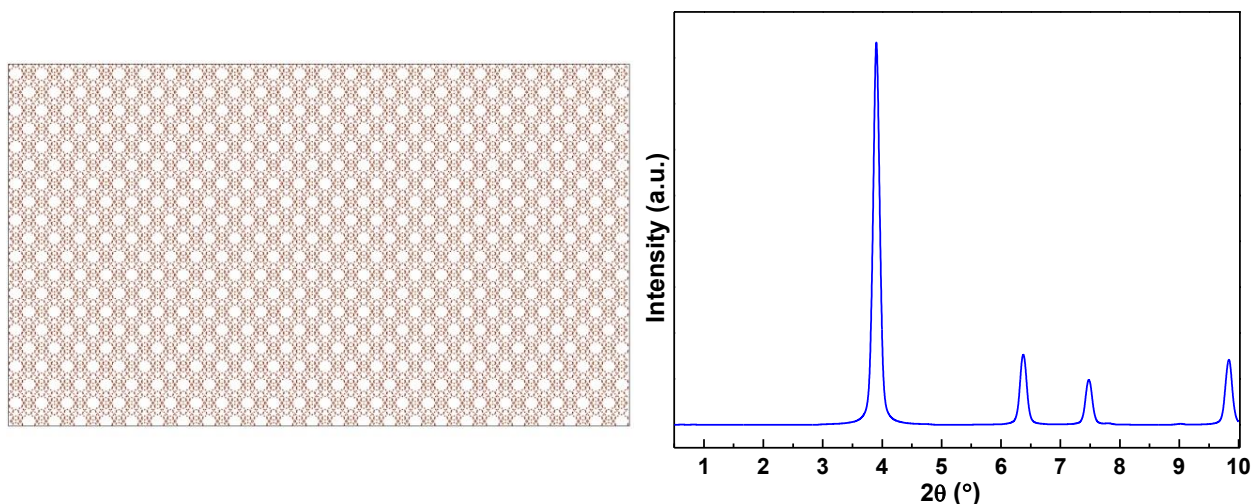
It should be noted that the apparent hump in the wide angle range in the *in situ* synchrotron XRD patterns of the surfactant-templated zeolites, centered between  $15$  and  $20^\circ 2\theta$  is due to the reflection of water molecules present in the *in situ* experiment (compare Supplementary Fig. 3 and 9).

### 3. Computational Simulations

Materials Studio software package has been employed to perform the simulations included in this section [Materials Studio, v. 6.0; Accelrys Inc., 2012]. To include an hexagonally ordered mesopore array crystal, a faujasitic supercell of  $411 \times 267 \times 34 \text{ \AA}$  was created from the original faujasitic unit cell (ICSD code: 24870. Cubic,  $Fd\bar{3}m$ ,  $a = 24.240 \text{ \AA}$ ). The simulated PXRD from the supercell matches that of the original cell and that of the herein studied USY sample (CBV720, Si/Al=15), see Supplementary Fig. 10. The size of the supercell was selected to fit the periodicity of the hexagonal mesostructure onto faujasitic periodicity.

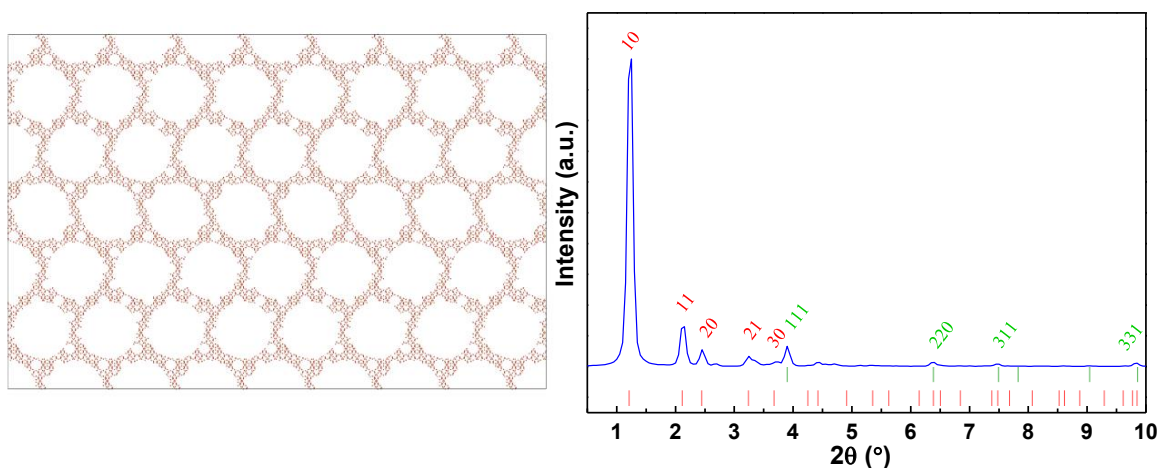
Two mesoporous model were built (Supplementary Fig. 11 and 12). The first one consisted of a perfectly ordered hexagonal array with pore to pore distance of  $5.142 \text{ nm}$  and a pore diameter of  $4.3 \text{ nm}$ . At high angle values, the PXRD fits the expected peaks for the faujasite, while at low angle the peaks featuring the

hexagonal arrangement of the mesopore appear. Supplementary Figure 11 shows an indexation of the simulated profile considering both contributions.



**Supplementary Figure 10.** Faujasite supercell (left) and simulated XRD pattern ( $\lambda = 0.95390 \text{ \AA}$ ) (right).

It must be considered that when the supercell is created, its size is adjusted to get the best possible fit with the periodicity of the faujasite. However, as a perfect match is not available unless unaffordable extremely large supercells are employed, it creates a small mismatch between the original faujasitic structure and the y-edge of the supercell that depends on the size of the supercell and the periodicity of the mesostructure (mismatch ca.  $0.55 \text{ \AA}$ ). Consequently, some minor satellite peaks appear into the simulated diffractograms. Similar phenomena has been previous described for mesoporous structural models created for amorphous silica.<sup>3</sup>

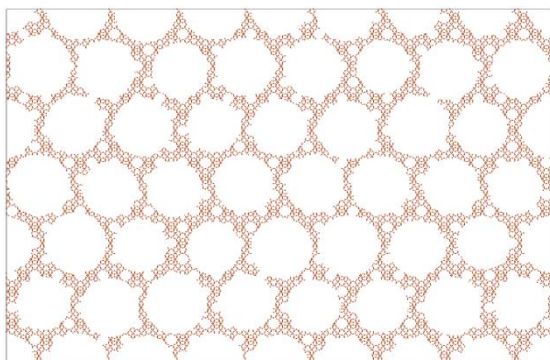


**Supplementary Figure 11.** Faujasitic supercell with a perfectly ordered hexagonal mesopore array (left) and the corresponding simulated XRD pattern ( $\lambda = 0.95390 \text{ \AA}$ ) (right).

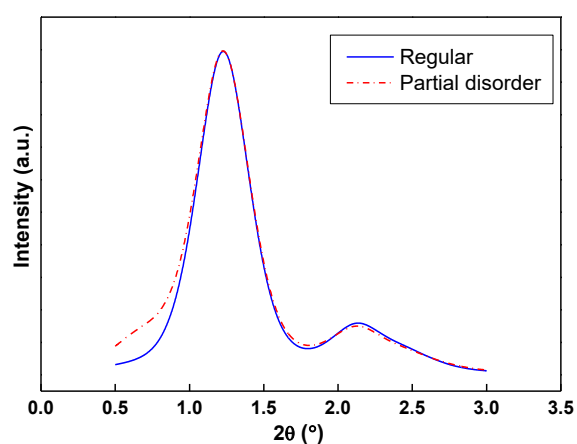
In order to reproduce the low angle broad peaks belonging to the ordering of the mesopores, diffractograms were simulated in which the domain size of the ordered mesophase was progressively decreased (Fig. 2c in the main paper). It should be emphasized that the mesopore domain induced peak broadening should only affect the low angle peaks, as the faujasite domain size is far bigger. Thus, only low angle range is meaningful in this comparison.

Simulated PXRD for a micropore size domain of 150 nm from the second model (*i.e.* partially disordered hexagonal mesopore array: random distribution of the pore-to-pore distance and diameter between 4.9-5.3

and 4.0-4.6 nm, Supplementary Fig. 12) also reproduces fairly well the features of the experimental sample and it is comparable with the pattern produced perfectly ordered or regular mesopore array (Supplementary Fig. 14).



**Supplementary Figure 12.** Faujasitic supercell with partially disordered hexagonal mesopore array.



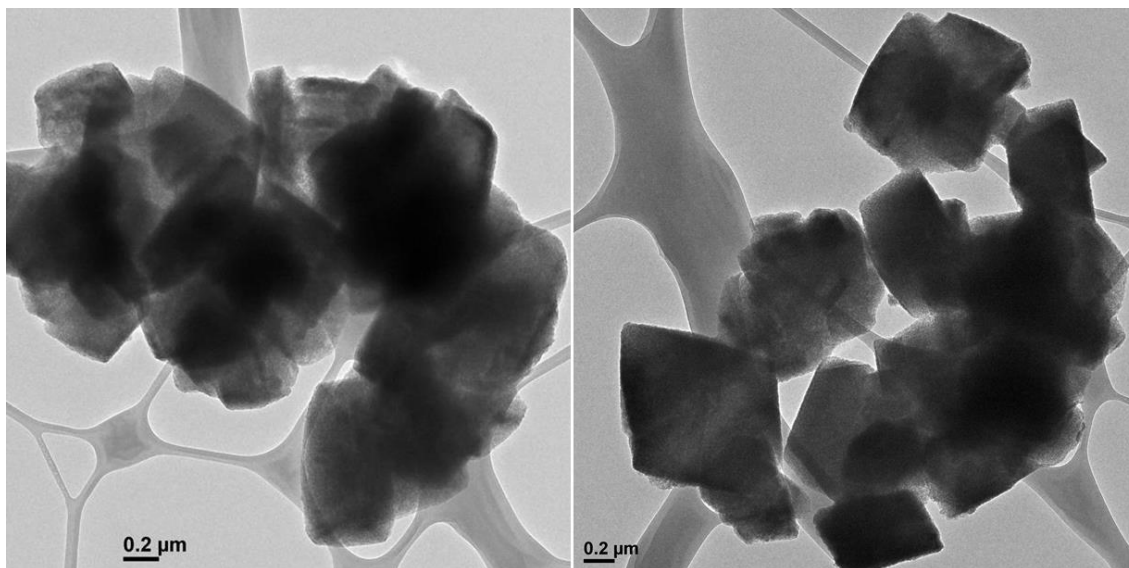
**Supplementary Figure 13.** Simulated XRD patterns for the Faujasitic supercell with a perfectly ordered (blue line) and partially disordered (red dotted line) hexagonal mesopore array using a 150 nm mesopore domain size.

#### 4. *Ex situ* characterization: N<sub>2</sub> physisorption and TEM analyses

**Supplementary Table 1.** Textural properties of the *ex situ* calcined surfactant-templated USY zeolites after different times of treatment.

Sample	V <sub>micro</sub> <sup>[a]</sup> (cm <sup>3</sup> g <sup>-1</sup> )	V <sub>meso</sub> <sup>[b]</sup> (cm <sup>3</sup> g <sup>-1</sup> )	V <sub>tot</sub> <sup>[c]</sup> (cm <sup>3</sup> g <sup>-1</sup> )	S <sub>BET</sub> <sup>[d]</sup> (m <sup>2</sup> g <sup>-1</sup> )
USY	0.30	0.20	0.50	669
1 min	0.23	0.29	0.52	677
2 min	0.24	0.29	0.53	709
4 min	0.24	0.30	0.54	739
5 min	0.23	0.33	0.56	779
10 min	0.23	0.36	0.59	780
20 min	0.21	0.36	0.57	763
30 min	0.20	0.40	0.60	802
60 min	0.19	0.44	0.63	830
120 min	0.17	0.48	0.65	822

[a] Micropore volume determined by NL-DFT from the adsorption branch of the isotherms shown in Fig. 3 (main paper). [b] Mesopore volume calculated by subtracting the micropore volume from the total pore volume. [c] Total pore volume obtained by NL-DFT at  $P/P_0 = 0.99$ . [d] BET surface area.

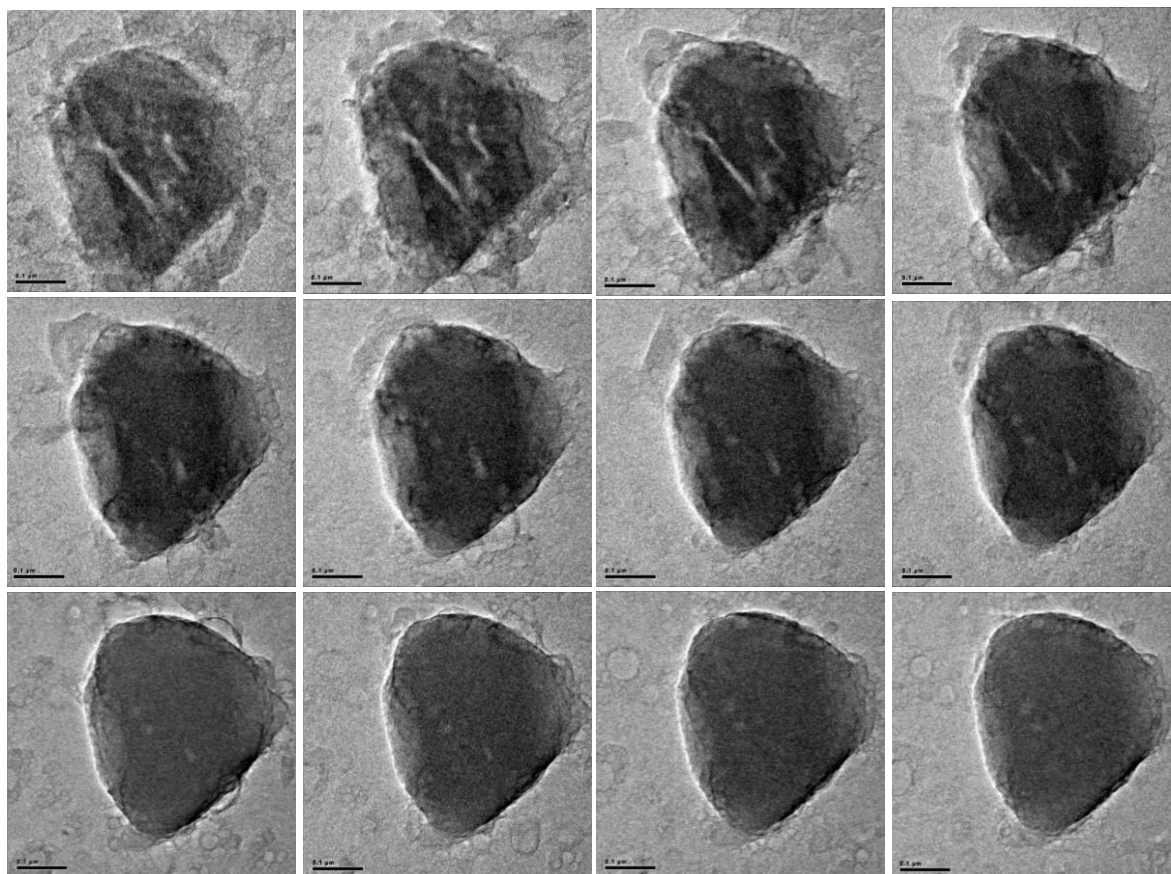


**Supplementary Figure 14.** TEM images at low magnification of a surfactant-templated USY zeolite ( $\text{Si}/\text{Al} = 15$ ) treated for 60 min.

## 5. Liq-TEM videos and images

### 5.1 Mesostructuring process of USY zeolite ( $\text{Si}/\text{Al} = 15$ )

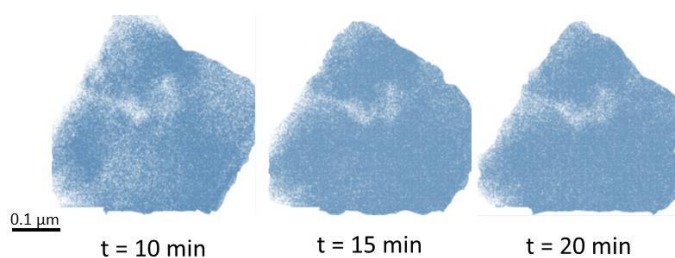
Recorded Liq-TEM observation of the surfactant-templating of the USY zeolite ( $\text{Si}/\text{Al} = 15$ ) is shown in **Supplementary Movie 1**.



**Supplementary Figure 15.** Frames from video shown in Supplementary Movie 1 with time intervals of 60 s from recorded *in situ* Liq-TEM observation of the surfactant-templating of USY zeolite (Si/Al = 15). Scale bar = 0.1  $\mu\text{m}$ .

### 5.2 Treatment of a USY zeolite (Si/Al = 40) with water.

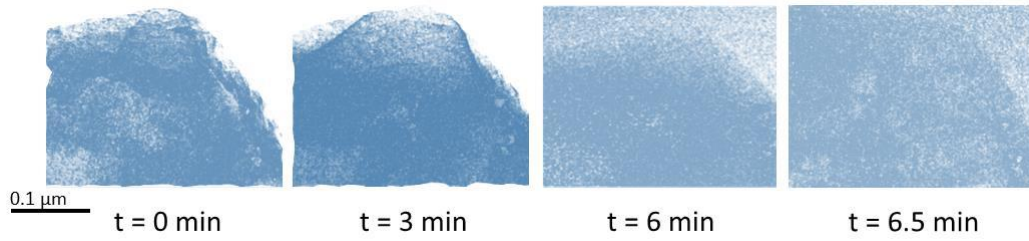
Recorded Liq-TEM observation of the USY (Si/Al=40) zeolite in water is shown in **Supplementary Movie 2**.



**Supplementary Figure 16.** Digital treated frames from recorded *in situ* Liq-TEM observation (Supplementary Movie 2) at different times of USY (Si/Al=40) zeolite in water.

### 5.3 Treatment of a USY zeolite (Si/Al =40) with a NaOH solution

Recorded Liq-TEM observation of the basic treatment of the USY (Si/Al=40) zeolite in absence of surfactant is shown in **Supplementary Movie 3**.



**Supplementary Figure 17.** Digital treated frames from recorded *in situ* Liq-TEM observation (Supplementary Movie 3) at different times of the basic treatment of USY (Si/Al=40) zeolite in absence of surfactant.

## 6. Study of the sample heating by electron beam

### 6.1 Electron energy loss

The “collision” of incoming electrons from the beam can cause an increase of the sample temperature, which happens by electron energy transfer to the sample. Amongst the theoretical models, modified Bethe function for electrons<sup>4</sup> has been used to provide good approximation on the energy ( $E$ ) loss of the electrons in function of sample thickness ( $x$ ) in electron microscopy (TEM) experiments:<sup>5</sup>

$$-\frac{dE}{dx} = 2\pi N_a r_e^2 m_e c^2 \rho \frac{Z}{A} \frac{1}{\beta} \left[ \ln \frac{\tau^2(\tau+2)}{2(I/m_e c^2)^2} + F(\tau) - \delta - 2 \frac{C}{Z} \right] \quad (\text{eq.1})$$

The above equation relates the characteristics of the incoming electrons (classical radius ( $r_e$ ), mass ( $m_e$ ), speed ( $v$ ) and kinetic energy ( $\tau$ ) in units of  $m_e c^2$ ) and absorber material (density ( $\rho$ ), atomic number ( $Z$ ) and atomic weight ( $A$ )). Besides,  $N_a$  is the Avogadro's number,  $\beta$  is the ratio between  $v$  and the speed of the light ( $c$ ).  $\delta$  and  $C$  are the density correction and shell correction, respectively, which are important for intermediate and high electron energies ( $< 0.5$  MeV), then not considered in further calculations.  $I$  is the mean excitation energy for energy loss in the absorber material, which value can be approximately calculated by:<sup>4b</sup>

$$I = 9.76Z + \frac{58.8}{Z^{0.19}} \quad (\text{eq.2})$$

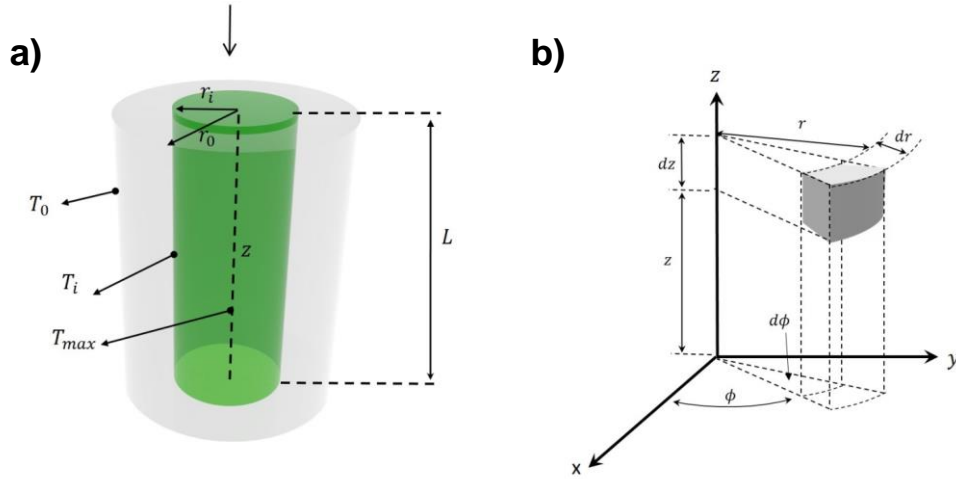
$F(\tau)$  is the Bethe correction function, which is dependent of the incoming particle, in the case electrons, which means:

$$F(\tau) = 1 - \beta^2 + \frac{\tau^2 - (2\tau+1) \ln 2}{(\tau+1)^2} \quad (\text{eq.3})$$

Eq.1 implies electron energy loss of  $1.29 \times 10^{-11} \text{ Jm}^{-1}$  for water,  $2.17 \times 10^{-11} \text{ Jm}^{-1}$  for silicon nitrate (substrate) and  $6.6 \times 10^{-14} \text{ J/m}$  for zeolites (assuming an average  $Z$  of 34.5 and  $\rho \sim 0.74 \text{ g cm}^{-3}$ ).

### 6.2 Sample heating by the electrons

The irradiated volume in a thin sample can be approximated to a cylinder of radius  $r$ , concentric to an bigger volume of radius ( $r_0$ ) (illuminated volume plus an non-illuminated volume), see Supplementary Fig. 18.



**Supplementary Figure 18.** (a) Scheme of the volumetric interaction part of the sample by electron beam (green) and surroundings (gray). (b) Cylindrical coordinate system for the general heat conduction equation.

Assuming the thermal conduction in the thin sample in vacuum is mainly due to the conduction, *i.e.* no considerable radiation and convection, the general form of two-dimensional heat conduction equation in the cylindrical form can be applied:<sup>5</sup>

$$\frac{1}{r} \frac{\partial}{\partial r} \left( r \frac{\partial T}{\partial r} \right) + \frac{1}{r^2} \frac{\partial^2 T}{\partial \phi^2} + \frac{\partial^2 T}{\partial z^2} + \frac{q_G}{k} = \frac{1}{\alpha} \frac{\partial T}{\partial t} \quad (\text{eq.4})$$

where  $q_G$  is the rate of energy generation within the volume,  $k$  the thermal conductivity,  $T$  the temperature,  $t$  the time and  $r, z, \phi$  the cylindrical coordinates (Supplementary Fig. 18b). Then, the heat conduction regime can be separated in two parts:

**(a) Area without beam illumination (gray area in the Supplementary Fig. 18a)**

For the non-illuminated area, the heat flow can be approximated by only radial flow ( $\partial^2 T / \partial \phi^2 = 0$ ,  $\partial^2 T / \partial z^2 = 0$ ), with no time dependence (*i.e.*, steady-state,  $\partial T / \partial t = 0$ ) and no energy generation, the resulting steady-state conduction equation for cylindrical coordinates is:

$$\frac{d}{dr} \left( r \frac{dT}{dr} \right) = 0 \quad (\text{eq.5})$$

Integrating once with respect to radius gives:

$$r \frac{dT}{dr} = C_1 \quad (\text{eq.6})$$

or

$$\frac{dT}{dr} = \frac{C_1}{r} \quad (\text{eq.7})$$

A second integration gives  $T = C_1 \ln r + C_2$ . The constants of integration can be determined from the boundary conditions ( $T_i = C_1 \ln r_i + C_2$  at  $r = r_i$  and  $T_0 = C_1 \ln r_0 + T_i - C_1 \ln r_i$  at  $r = r_0$ ), then:

$$C_2 = T_i - C_1 \ln r_i \quad (\text{eq.8})$$

And

$$C_1 = \frac{(T_0 - T_i)}{\ln(r_0/r_i)} \quad (\text{eq.9})$$

The rate of heat transfer by conduction ( $q_k$ ) from inner cylinder (beam illuminated) and the outer one can be calculated by:

$$q_k = -kA \frac{dT}{dr} = -k(2\pi rL) \frac{C_1}{r} \quad (\text{eq.10})$$

Where  $A$  is the area of the cylinder. Values of  $q_k$  can be calculated according to the experimental parameters ( $q_k = J\pi r_i^2 n(dE/dx)L$ , where  $J$  is the current,  $L$  the cylinder height and  $n$  the number of electrons). By using eq. 10 in the eq. 9 implies in the temperature distribution from the  $r_i$  to  $r_0$ :

$$T = T_0 + \frac{q_k}{2\pi kL} \ln\left(\frac{r_0}{r}\right) \quad (\text{eq. 11})$$

Consequently, the temperature in the interface between beam illuminated and non-illuminated areas is obtained when  $r = r_i$ .

**(b) Area with beam illumination (green area in the Supplementary Fig. 18b)**

Assuming the same relations by the eq.5, but with heat generation, it is obtained:

$$r q_G = -k \left( \frac{dT}{dr} + \frac{d^2T}{dr^2} \right) \quad (\text{eq.12})$$

where  $q_G$  is the heat transfer flux density and can be calculated according to the experimental parameters ( $q_G = q_k/\pi r_i^2 L$ ). The integration of eq.12 yields:

$$\frac{r^2 q_G}{2} = -kr \frac{dT}{dr} + C_3 \quad (\text{eq.13})$$

And

$$T = -\frac{r^2 q_G}{4k} + C_4 \quad (\text{eq.14})$$

In order to satisfy the boundary conditions  $dT/dr = 0$  at  $r = 0$  and  $r = r_i$  is  $T_i$ ,  $C_3$  must be zero and  $C_4 = (q_G r_i^2 / 4k) + T$ . Then, the maximum temperature ( $T_{max}$ ) at  $r = 0$  is:

$$T_{max} = T_i + \frac{q_G r_0^2}{4k} \quad (\text{eq.15})$$

And the temperature distribution:

$$T = T_i + \frac{q_G r_0^2}{4k} \left[ 1 - \left( \frac{r}{r_i} \right)^2 \right] \quad (\text{eq.16})$$

In order to satisfy the boundary conditions  $dT/dr = 0$  at  $r = 0$  and  $r = r_i$  is  $T_i$ ,  $C_3$  must be zero and  $C_4 = (q_G r_i^2 / 4k) + T$ . Then, the maximum temperature ( $T_{max}$ ) at  $r = 0$  is:

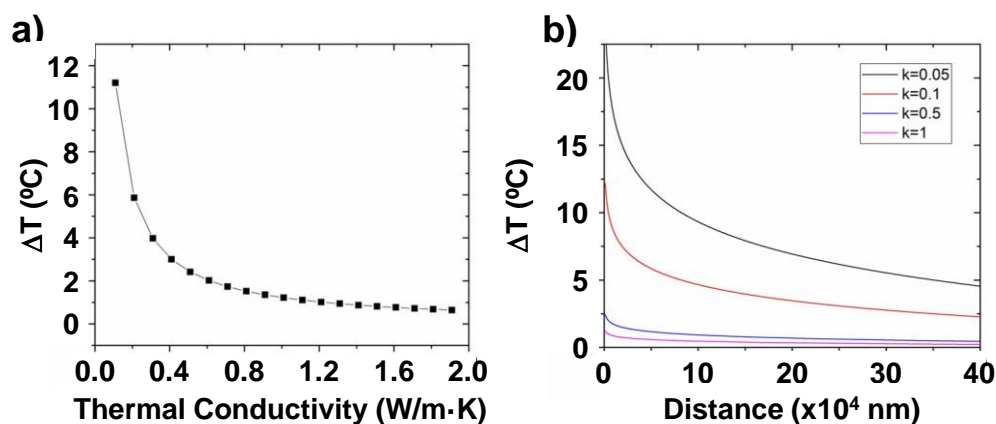
$$T_{max} = T_i + \frac{q_G r_i^2}{4k} \quad (\text{eq.17})$$

And the temperature distribution:

$$T = T_i + \frac{q_G r_i^2}{4k} \left[ 1 - \left( \frac{r}{r_i} \right)^2 \right] \quad (\text{eq.18})$$

Consequently, the temperature profile in a two dimension is determinate according to energy generation within the sample by the electron beam.

Assuming a typical *in situ* Liq-TEM experiment by using an electron acceleration voltage of 300 keV, beam size radius ( $r$ ) of  $1.5 \times 10^{-6}$  m (illuminated area,  $r_i$ ), current density ( $j$ ) of  $2500 \text{ A m}^{-2}$  and sample thickness ( $L$ ) of 100 nm. Supplementary Fig. 19 shows the graphic of maximum temperature induced in the sample by conductivity of electron energy loss and the temperature profile according to the distance from the maximum temperature region (z-axis in the Supplementary Fig. 18). The calculated maximum temperatures evidence considerable temperature variations ( $\Delta T > 10 \text{ }^\circ\text{C}$ ) only for materials with thermal conductivity less than  $0.3 \text{ W/m.k}$ , which is not the case of water ( $0.58 \text{ W m}^{-1} \text{ K}^{-1}$ ), silicon nitride ( $\sim 2 \text{ Wm}^{-1}\text{K}^{-1}$ ) or the zeolite particles ( $0.5\text{-}2 \text{ Wm}^{-1}\text{K}^{-1}$ ).<sup>6</sup> Due to these materials thermal conductivity, it is not expected temperature variations of more than 5.6 K in the *in situ* Liq-TEM studies. Equivalent temperature variation was also determinate by Zheng *et al.* for *in situ* Liq-TEM study by using similar experimental conditions.<sup>6b</sup>



**Supplementary Figure 19.** (a) Maximum temperature induced by electron energy loss in the sample by thermal conductivity. (b) Temperature variation profile from the maximum temperature (center of the cylinder in Supplementary Figure 19a) to surrounds for selected thermal ( $k = 0.2, 0.4, 0.6, 0.8$  and  $1 \text{ W m}^{-1} \text{ K}^{-1}$ ).

## References

- [1] F. Fauth, I. Peral, C. Popescu, M. Knapp, *Powder Diffraction* **2013**, 28, S360.
- [2] a) G. Williamson, W. H. Hall, *Acta Metall.* **1953**, 1, 22; b) V. D. Mote, Y. Purushotham, B. N. Dole, *J. Theoret. Appl. Phys.* **2012**, 6:6, 1; b) H. S. Cho, K. Miyasaka, H. Kim, Y. Kubota, M. Takata, S. Kitaqawa, R. Ryoo, O. Terasaki, *J. Phys. Chem. C* **2012**, 116, 25300.
- [3] Y. Jing, L. Wei, Y. Wang, Y. Yu, *Chem. Eng. J.* **2013**, 220, 264.
- [4] a) H. Bethe, *Annalen der Physik* **2006**, 397, 1930; b) E. Kamaratos, *Chem. Rev.* **1984**, 84, 561.
- [5] a) L. Reimer, H. Kohl, *Transmission Electron Microscopy: Physics of Image Formation*, ISBN: 9780387347585, Springer, NY, **2008**; b) H. Zheng, S.A. Claridge, A. M. Minor, P. A. Alivisatos, U. Dahmen, *Nano Letters* **2009**, 9, 2460; c) R. F. Egerton, P. Li, M. Malac, *Micron* **2004**, 35, 399.
- [6] a) F. Kreith, R.M. Manglik, M.S. Bohn, *Principles of Heat Transfer*, SI Edition, ISBN: 9781439061862, Cengage Learning, **2012**; b) T. L. Bergman, F. P. Incropera, D. P. DeWitt, A. S. Lavine, *Fundamentals of Heat and Mass Transfer*, ISBN: 9780470501979, Wiley, **2011**.